


Crisis-induced flow reversals in magnetoconvectionManojit Ghosh[✉],* Ankan Banerjee, and Pinaki Pal[†]*Department of Mathematics, National Institute of Technology, Durgapur 713209, India* (Received 23 August 2020; revised 5 May 2021; accepted 23 June 2021; published 30 July 2021)

We report the occurrence of flow reversals induced by the attractor-merging crisis in Rayleigh-Bénard convection of electrically conducting low-Prandtl-number fluids in the presence of a uniform external horizontal magnetic field. The simultaneous collision of two coexisting chaotic attractors with an unstable fixed point and its associated stable manifold takes place in the higher-dimensional phase space of the system, leading to a single merged chaotic attractor. The effect of strength of the magnetic field on the flow reversal phenomena is also explored in detail.

DOI: [10.1103/PhysRevE.104.015111](https://doi.org/10.1103/PhysRevE.104.015111)**I. INTRODUCTION**

Flow reversals have long been a topic of interest to researchers due to their relevance to various geophysical and industrial applications. For example, Earth's geomagnetic field has gone through numerous reversals of polarity in the last 10 million years (four or five reversals per million years on an average). Industrial applications of flow reversals include the vacuum arc remelting (VAR) refining process which is used to remove impurities and porosity from ingots [1,2]. The appearance of flow reversals in VAR gives rise to a change in the pool shape and influences the ingot structure. Thus, great effort is made to minimize the effect of flow reversals in VAR. Flow reversals are also observed in large-scale fluid motion occurring in the ocean and atmosphere [3]. To understand the mechanism of reversal phenomena, researchers often rely on some simplified models such as Rayleigh-Bénard convection (RBC). The geometry of RBC is quite simple and consists of a thin layer of fluid confined between two horizontal parallel plates subjected to a vertical temperature gradient [4]. Two control parameters, namely, the Rayleigh number Ra (the strength of the buoyancy) and the Prandtl number Pr (the ratio of the kinematic viscosity and thermal diffusivity of the fluid), control the dynamics of RBC. The occurrence of flow reversals in RBC has also been reported in many experimental and numerical studies where reversals are related to the large-scale circulations appearing in turbulent convection [5–11]. However, in most of these studies the fluids under consideration have $Pr \geq 0.7$. In contrast, flow reversals in low- Pr fluids (such as liquid metals, which are more relevant in the context of industrial applications) are relatively less studied. Yanagisawa and coworkers reported the occurrence of flow reversals in RBC of low- Pr fluids such as liquid metals in the presence of a horizontal magnetic field [12–14]. They observed random flow reversals in their experimental study

when $Ra/Q \approx 10$, where Q is the Chandrasekhar number, measures the strength of the Lorentz force [12]. In their numerical study, they reported a transition between four-roll and five-roll structures, which causes the flow reversals [14].

Recently, Mannattil *et al.* numerically studied the flow reversal phenomena appearing in infinite- Pr and zero- Pr fluids and showed that they are very different from each other [15]. They reported that for zero- Pr reversals, the velocity nonlinearity dominates all other terms, while the most dominating term for infinite- Pr reversals is the nonlinearity present in the energy equation. The study also emphasized the applicability of low-dimensional models to capture the reversal dynamics in detail and reported that the dynamics associated with zero- Pr reversals can be captured with a deterministic low-dimensional model proposed by Pal *et al.* [16]. It is interesting to note that similar deterministic low-dimensional models are also used to explore the nonlinear properties of low- Pr RBC in the presence of magnetic field [17–19]. However, to the best of our knowledge, the nonlinear dynamics of flow reversals appearing in low- Pr fluids in the presence of external magnetic field have not been explored yet. We address this issue in the present study by considering the alignment of the external magnetic field along the horizontal direction. We first perform three-dimensional (3D) direct numerical simulations (DNSs) of the governing equations for this purpose. Then we construct a low-dimensional model from DNS data to investigate the reversal dynamics. Analysis of the model together with the support from DNSs reveals the presence of an attractor-merging crisis in the system which is found to cause the flow reversals.

Crises are global bifurcations which occur when a chaotic attractor collides with an unstable periodic orbit (UPO) and its stable manifold [20,21]. An attractor-merging crisis generally occurs in systems with symmetries where two or more chaotic attractors merge together to form a single chaotic attractor as a system parameter is varied [21]. At the critical value of the control parameter, the precrisis attractors simultaneously touch their common basin boundary and collide with one or more UPOs to form the merged attractor. The attractor-merging crisis has also been observed in several numerical

*Present address: Jawaharlal Nehru Centre for Advanced Scientific Research, Jakkur P.O., Bangalore 560064, India.

[†]pinaki.pal@maths.nitdgp.ac.in

and experimental studies [22–26]. However, the mechanism of crisis may differ in higher-dimensional systems if an unstable time-independent equilibrium solution “zero” exists [21]. For example, consider the Lorenz system where three attractors (one chaotic attractor and two fixed point attractors) coexist in a certain parameter range. As the parameter is varied, the chaotic attractor collides with the basin boundary of the fixed point attractors and gives rise to a chaotic transient [21]. In this paper, we characterize an attractor-merging crisis in RBC of low-Pr fluids in the presence of an external uniform horizontal magnetic field which leads to the flow reversals.

The rest of this paper is organized as follows: Sec. II describes the mathematical formulation of the problem. The results of the DNSs are discussed in Sec. III. Section IV is devoted to portraying the reversal mechanism using a reduced model constructed from DNS data. The effect of Q and Pr on the reversal dynamics is detailed in Sec. V, and some concluding remarks are drawn in Sec. VI.

II. PHYSICAL SYSTEM AND GOVERNING EQUATIONS

We consider a classical Rayleigh-Bénard geometry in which an infinitely extended thin horizontal layer of electrically conducting fluids is confined between two thermally and electrically conducting horizontal plates in the presence of an external uniform horizontal magnetic field $\mathbf{B}_0 \equiv (0, B_0, 0)$. The bottom plate is heated uniformly to maintain a steady temperature gradient $\beta = \Delta T/d = (T_l - T_u)/d$ across the fluid layer, where T_u and T_l are, respectively, the temperature of the upper and lower plates with $T_l > T_u$. We consider low-Pr fluids for which the magnetic Prandtl number Pm (the ratio of the kinematic viscosity and magnetic diffusivity) is vanishingly small. Therefore, we consider quasistatic approximation (Pm \rightarrow 0). Following this approximation, the dimensionless equations which govern the convective motion of the fluid under Boussinesq approximation are given by

$$\partial_t \mathbf{v} + (\mathbf{v} \cdot \nabla) \mathbf{v} = -\nabla \pi + \nabla^2 \mathbf{v} + \text{Ra} \theta \hat{\mathbf{e}}_3 + Q \partial_y \mathbf{b}, \quad (1)$$

$$\nabla^2 \mathbf{b} = -\partial_y \mathbf{v}, \quad (2)$$

$$\text{Pr}[\partial_t \theta + (\mathbf{v} \cdot \nabla) \theta] = v_3 + \nabla^2 \theta, \quad (3)$$

$$\nabla \cdot \mathbf{v} = 0, \quad \nabla \cdot \mathbf{b} = 0. \quad (4)$$

In the above set of equations, $\mathbf{v} \equiv (v_1, v_2, v_3)$, $\mathbf{b} \equiv (b_1, b_2, b_3)$, θ , and π are, respectively, the convective velocity field, the induced magnetic field, the convective temperature field, and the modified pressure field. $\hat{\mathbf{e}}_3$ is the unit vector along the vertical direction opposite the gravitational acceleration $\mathbf{g} \equiv (0, 0, g)$. We choose the viscous diffusion timescale d^2/ν as the characteristic timescale to perform the nondimensionalization procedure. Three dimensionless parameters are the Rayleigh number $\text{Ra} = \alpha \Delta T g d^3 / \kappa \nu$, the Chandrasekhar number $Q = B_0^2 d^2 / \nu \lambda \rho_0$, and the Prandtl number $\text{Pr} = \nu / \kappa$. The coefficients α , κ , ν , λ , and ρ_0 are, respectively, the coefficient of the volume expansion, thermal diffusivity, kinematic viscosity, magnetic diffusivity, and reference density of the fluid. Stress-free and perfectly thermally conducting bounding plates lead to the boundary conditions for the velocity field

and temperature field:

$$v_3 = \partial_z v_1 = \partial_z v_2 = \theta = 0, \quad z = 0, 1. \quad (5)$$

On the other hand, electrically conducting plates give the boundary conditions for the magnetic field:

$$b_3 = \partial_z b_1 = \partial_z b_2 = 0, \quad z = 0, 1. \quad (6)$$

The presence of horizontal magnetic field destroys the $x \equiv y$ symmetry of the system [Eqs. (1)–(4)] and acts as an imperfection parameter [27]. However, the system retains the inversion symmetry, $x \rightarrow -x$, $y \rightarrow -y$, $v_1 \rightarrow -v_1$, $v_2 \rightarrow -v_2$, and $b_3 \rightarrow -b_3$, while other fields do not change sign [19]. Linear stability analysis of the system shows that the onset of convection is independent of both Q and Pr. Therefore, the critical Rayleigh number ($\text{Ra}_c = 27\pi^4/4$) and associated wave number ($k_c = \pi/\sqrt{2}$) are not different from the non-magnetic case. Now, to explore the effect of both Q and Pr on the higher order instabilities, we perform DNS, which is discussed in Sec. III.

III. DNS RESULTS

We use the pseudospectral code TARANG [28] to perform the DNS of the system [Eqs. (1)–(4)] together with the boundary conditions (5) and (6). In the simulation code, the independent fields, i.e., vertical velocity, vertical vorticity ω_3 , and temperature, are expanded using the set of orthogonal basis functions compatible with the boundary conditions. Thus, the expressions of v_3 , ω_3 , and θ in the Fourier space become

$$\begin{aligned} (v_3, \theta) &= \sum_{l,m,n} (W_{lmn}(t), T_{lmn}(t)) e^{i(lk_x x + mk_y y)} \sin(n\pi z), \\ \omega_3 &= \sum_{l,m,n} Z_{lmn}(t) e^{i(lk_x x + mk_y y)} \cos(n\pi z). \end{aligned} \quad (7)$$

W_{lmn} , Z_{lmn} , and T_{lmn} are the Fourier modes or amplitudes, with l , m , and n being the non-negative integers. k_x and k_y are the horizontal wave numbers along the x and y directions, respectively. For the present simulation, we choose

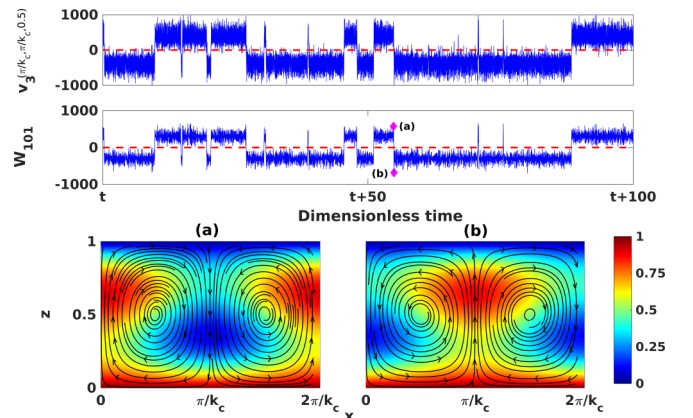


FIG. 1. The top two panels show the time series of $v_3(\pi/k_c, \pi/k_c, 0.5)$ and the dominant Fourier mode W_{101} from DNS at $r = 7$ for $Q = 100$ and $\text{Pr} = 0.025$. The bottom panels display the convective flow profile: before the reversal (left) and after the reversal (right).

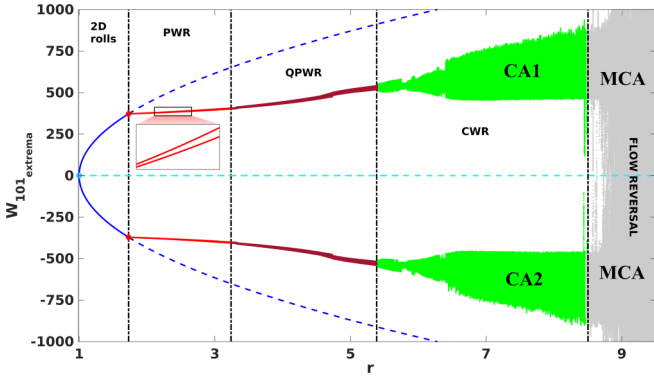


FIG. 2. The bifurcation diagram for $Q = 100$ and $Pr = 0.025$ shows the merging of chaotic attractors (CA1 and CA2) into a single attractor (MCA). The dashed cyan (lighter gray) curve is the mediating saddle, the unstable conduction state M. The solid cyan (lighter gray) circle and red (medium gray) diamonds denote the pitchfork bifurcation and Hopf bifurcations.

$k_x = k_y = k_c = \pi/\sqrt{2}$, where k_c is the critical wave number for the onset of convection. Simulations are performed in a square simulation box of size $(2\pi/k_c) \times (2\pi/k_c) \times 1 \equiv 2\sqrt{2} \times 2\sqrt{2} \times 1$ using random initial conditions. Periodicity is considered for all the fields along horizontal directions. This simulation box rules out roll-merging phenomena reported by Yanagisawa *et al.* [12,14] [see ansatz (7)], but it is a reasonable representation of flow in confined geometries, while allowing more numerical exploration than would be possible if explicit sidewall boundaries were introduced. We consider a maximum of 64^3 spatial grid resolution, although most of the simulations are carried out using 32^3 spatial grid resolution. A fourth order Runge-Kutta integration scheme with the Courant-Friedrichs-Lewy condition is used for time advancement with the time step $\delta t = 0.001$. We introduce a new parameter in the subsequent discussion, the reduced Rayleigh number ($r = Ra/Ra_c$), where Ra_c is the critical Rayleigh number for the convection onset.

We perform extensive DNSs for $Pr = 0.025$ by varying the values of Q and r in the ranges of $10 \leq Q \leq 500$ and $1 \leq r \leq 100$, respectively. We find two different routes to chaos, namely, period-doubling, corresponding to small Q , and quasiperiodic for higher Q , as reported in Refs. [18,29]. To discern the fate of the chaotic attractor, we fix the Q and gradually increase r . We notice the occurrence of flow reversals as r crosses a critical value depending on Q . Figure 1 shows the reversal phenomena at $r = 7$ for $Q = 100$. The top two panels in Fig. 1 display the time evolution of vertical velocity at $(\pi/k_c, \pi/k_c, 0.5)$ and dominant Fourier mode W_{101} . Both time series change sign frequently, indicating the reversal phenomena. The bottom panels in Fig. 1 show the velocity and temperature fields corresponding to two consecutive instants: before the reversal at $t = 104.8$ (left) and after the reversal at $t = 104.9$ (right). Now, to understand the origin of these reversals, we construct a low-dimensional model from the DNS data. The derivation and results of the reduced model are discussed in Sec. IV.

IV. REDUCED MODEL RESULTS

We construct a low-dimensional model from the DNS data following the method described in Ref. [30]. The basic idea is to identify the set of large-scale Fourier modes which principally contribute to the total energy. Following the method, we identify 8 large-scale vertical velocity modes ($W_{101}, W_{111}, W_{301}, W_{311}, W_{202}, W_{022}, W_{121}, W_{222}$), 13 vertical vorticity modes ($Z_{010}, Z_{210}, Z_{220}, Z_{230}, Z_{111}, Z_{121}, Z_{301}, Z_{311}, Z_{012}, Z_{202}, Z_{212}, Z_{222}, Z_{030}$), and 9 temperature modes ($T_{101}, T_{111}, T_{301}, T_{311}, T_{202}, T_{022}, T_{121}, T_{222}$, and T_{002}). Projecting the hydromagnetic system [Eqs. (1)–(4)] on these modes, we obtain 30 coupled nonlinear ordinary differential equations, which is our low-dimensional model. We analyze the model in detail using open-source software, XPPAUT [31], to get insight into the flow reversal phenomena. Note that in deriving the low-dimensional model we choose only the real part of the Fourier modes, which is consistent with the DNS results. As a result, we do not observe the traveling roll solution which was observed by Paul *et al.* in RBC in the absence of magnetic

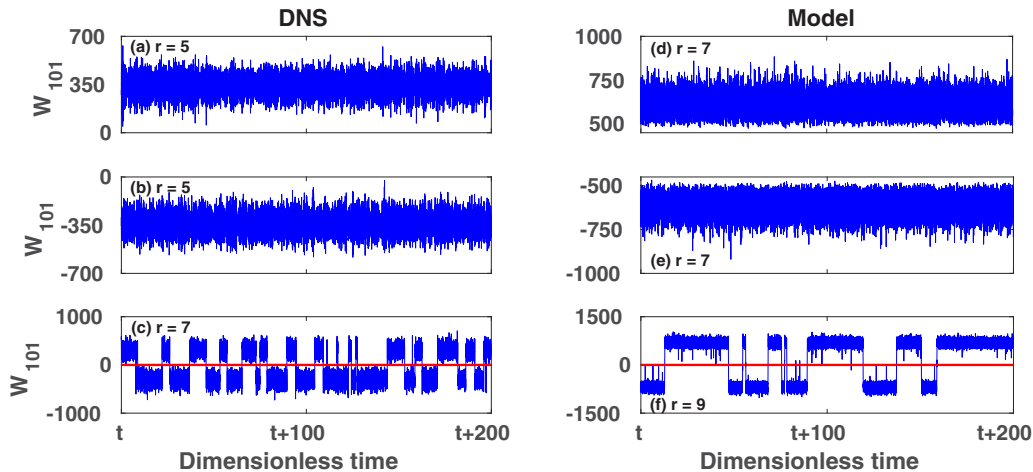


FIG. 3. Time evolution of the dominant Fourier mode W_{101} before and after the attractor-merging crisis obtained from both DNS and the model for $Q = 100$ and $Pr = 0.025$.

TABLE I. Different flow regimes obtained from DNS and the model corresponding to three different Q and two different Pr.

Q	Flow patterns	Pr = 0.025		Pr = 0.1	
		DNS (r)	Model (r)	DNS (r)	Model (r)
100	2D rolls	1–1.68	1–1.72	1–5.82	1–10.78
	PWR	1.69–1.87	1.73–3.33	5.83–10.61	10.79–19.58
	QPWR	1.88–3.70	3.34–5.62	10.62–13.37	19.59–28.34
	CWR	3.71–5.43	5.63–8.31	13.38–17.67	28.35–31.49
	Flow reversals	≥ 5.44	≥ 8.32	≥ 17.68	≥ 31.5
300	2D rolls	1–5.74	1–4.18	1–14.17	1–31.78
	PWR	5.75–6.02	4.19–10.18	14.18–21.61	31.79–36.34
	QPWR	6.03–7.37	10.19–14.39	21.62–24.01	36.35–44.87
	CWR	7.38–16.99	14.40–23.43	24.02–80.54	44.88–46.60
	Flow reversals	≥ 17.00	≥ 23.44	≥ 80.55	≥ 46.61
500	2D rolls	1–12.87	1–8.17	1–22.78	1–46.39
	PWR	12.88–13.82	8.18–20.83		46.40–46.53
	QPWR	13.83–16.50	20.84–36.79	22.79–34.73	46.54–69.79
	CWR	16.51–58.19	36.80–47.21	≥ 34.74	69.80–77.34
	Flow reversals	≥ 58.20	≥ 47.22		≥ 77.35

field [32]. Furthermore, in the current study the presence of magnetic field along the y direction suppresses the growth of W_{011} . The linear growth of W_{101} is stopped by transferring the energy to the wavy roll mode in the direction of the y axis (Z_{010}). Other modes are chosen following the nonlinear corrections using the terms $(\mathbf{v} \cdot \nabla) \mathbf{v}$ and $(\mathbf{v} \cdot \nabla) \theta$ in Eqs. (1) and (3), respectively.

To gain insight into the reversal dynamics, we first construct a bifurcation diagram using the model. Figure 2 shows the bifurcation diagram for $Q = 100$ and Pr = 0.025. From Fig. 2, we see that convection sets in at $r = 1$ through a supercritical pitchfork bifurcation in the form of steady two-dimensional (2D) rolls [blue (dark gray) curves] and the unstable conduction state [dashed cyan (lighter gray) curve] continues to exist for higher r . At $r = 1.73$, both 2D roll branches lose their stability via supercritical Hopf bifurcations, and stable limit cycles appear, which are also called the periodic wavy roll (PWR) solutions. Note that this Hopf bifurcation is a secondary bifurcation of convection through which time dependency enters in the system [18,33,34]. The extremum of the limit cycles are shown with the red (medium gray) curves. At $r = 3.345$, the limit cycles become unstable through Neimark-Sacker bifurcations, and quasiperiodicity appears in the system, followed by the chaos. The quasiperiodic and chaotic solutions, also known as quasiperiodic wavy rolls (QPWRs) and chaotic wavy rolls (CWRs), are shown with the brown (darker gray) and green (light gray) dots in Fig. 2. Both chaotic attractors (CA1 and CA2) grow in size with the increment in r , and at $r = r_{MC} \approx 8.32$ they collide with the mediating unstable conduction state M and merge together to form a single chaotic attractor (MCA). Immediately after this, we observe the occurrence of flow reversals in the system. This is a scenario of the attractor-merging crisis due to the presence of inversion symmetry in the system. The MCA is shown with the gray dots.

Figure 3 exhibits the time series of the dominant Fourier mode W_{101} before and after the attractor-merging crisis from DNSs and the model. Figures 3(a) and 3(b) display the pre-

crisis chaotic attractors (CA1 and CA2) from DNSs for $r = 5$, while those from the model are shown in Figs. 3(d) and 3(e) corresponding to $r = 7$. Figures 3(c) and 3(f) exhibit the postcrisis attractors (MCA) from DNSs and the model corresponding to $r = 7$ and $r = 9$, respectively. Figure 3 also establishes good qualitative agreement between the DNSs and model results. Table I presents a more detailed comparison of DNSs and model results for different values of Q and Pr. From Table I, good qualitative agreement between DNSs and the model results is observed, which validates the model. Therefore, we use the model further to detail the attractor-merging crisis.

To characterize the attractor-merging crisis we adopt a suitable Poincaré map, defined as the 29-dimensional hyperplane given by $W_{022} = 0$, with $\frac{d}{dt} W_{022} > 0$. Then we study the dynamics of the system by varying r for fixed Pr = 0.025 and $Q = 100$. It is interesting to note that the system always has a stationary saddle point M for $r > 1$. This saddle point is shown by the + symbol in Fig. 4. Figure 4(a) shows the projection of the symmetrically located precrisis chaotic attractors (CA1 and CA2) on the W_{101} - T_{101} plane with their basin of attraction for $r = 8.213$. Gray dots represent the

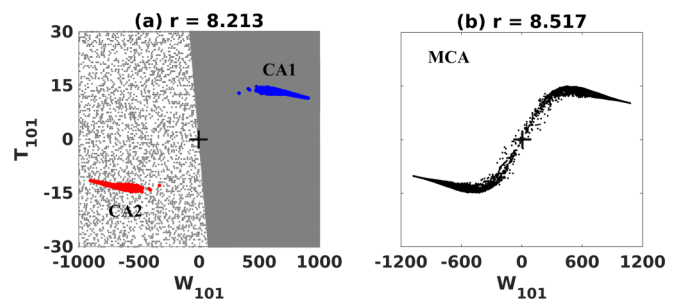


FIG. 4. (a) Projection of precrisis chaotic attractors CA1 and CA2 on the W_{101} - T_{101} plane with their basin of attraction for $Q = 100$ and Pr = 0.025. (b) Projection of postcrisis merged chaotic attractor MCA on the W_{101} - T_{101} plane for $Q = 100$ and Pr = 0.025.

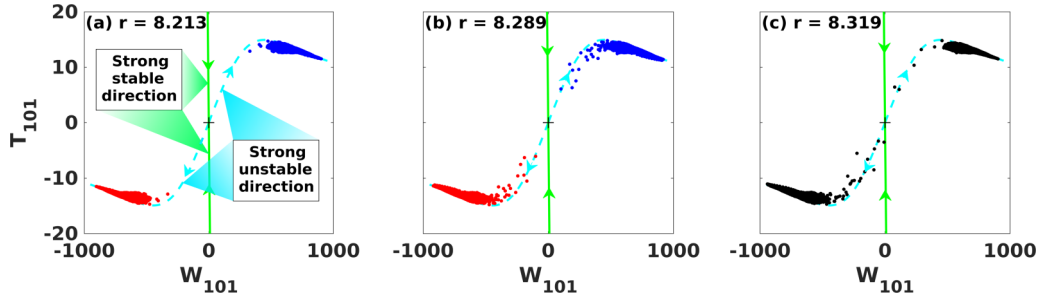


FIG. 5. Attractor-merging mechanism for $Q = 100$ and $Pr = 0.025$ corresponding to three different r . Blue (dark gray) and red (medium gray) dots in (a) and (b) are projections of CA1 and CA2 on the W_{101} - T_{101} plane. Black dots in (c) are the projection of MCA. Solid green (light gray) and dashed cyan (lighter gray) curves are the stable and unstable manifolds of mediating saddle M .

points in the basin of CA1, while the white background represents the basin of CA2. At $r = r_{MC}$ both CA1 and CA2 collide with the stable manifold of M and give rise to the merged attractor. Figure 4(b) displays the projection of the postcrisis attractor (MCA) on the W_{101} - T_{101} plane for $r = 8.517$.

The collision of CA1 and CA2 with the stable manifold of M is depicted in Fig. 5, in which projection of the chaotic attractors is shown together with the stable and unstable manifolds of M [solid green (light gray) and dashed cyan (lighter gray) curves respectively] corresponding to three different r . Comparing Figs. 5(a) and 5(b), we notice that both CA1 and CA2 grow in size with the increment in r . Also, both of them come closer to the stable manifold of M . Near $r = 8.319$, both CA1 and CA2 touch the stable manifold of M simultaneously and merge together to form the MCA [see Fig. 5(c)].

We further compute the variation of maximal Lyapunov exponent (MLE) near the crisis point to elucidate the scenario of the attractor-merging crisis. The MLE defines the degree of chaoticity of a system and shows universal behavior during the crisis phenomena [35]. During an attractor-merging crisis MLE shows a *knee* as the control parameter is varied [35]. As a result, the rate of change of MLE decreases significantly after the crisis. Figure 6(a) displays the variation of MLE for $Q = 100$ in the range $7 \leq r \leq 9$ computed using the model. The blue (dark gray) dots represent the MLE data calculated using XPPAUT, while black lines are the linear fit. From Fig. 6(a), we notice that MLE shows a knee at

$r = r_{MC} \approx 8.32$, which also ensures the occurrence of the attractor-merging crisis in the system.

V. EFFECT OF Q AND Pr ON FLOW REVERSALS

We also explore the effect of the strength of the magnetic field on reversal phenomena by computing the onset of flow reversals for different Q corresponding to $Pr = 0.025$. It is well known that the increment in Q suppresses the time-dependent solutions at the onset and enhances the regime of 2D rolls in low- Pr RBC [17,18]. As a result, the scenario of the attractor-merging crisis which causes the reversals is delayed to the higher values of r as we increase Q . In contrast, the reversals occur near the onset for small Q . Figure 6(b) shows the onset of flow reversals obtained from DNSs corresponding to different values of Q for $Pr = 0.025$. We observe that the reversal phenomena do not occur until higher r with the increment in Q following a power law.

We use the model further to explore the influence of Pr on the reversal dynamics. Figure 7 displays the appearance of different flow regimes on the Q - r plane corresponding to two different Pr . By comparing Figs. 7(a) and 7(b), we observe that manipulation of Pr does not cause any qualitative change in the flow dynamics, but it does bring quantitative changes in the flow regimes. From Fig. 7, we notice that with the increment in Pr the regions of 2D rolls and QPWR expand as Q increases, while the region of PWR shrinks and eventually

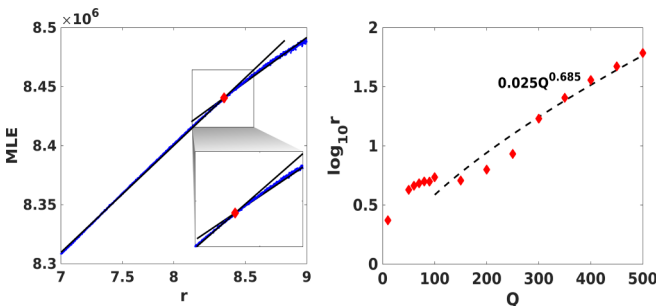


FIG. 6. (a) Variation of MLE near the crisis point for $Q = 100$, $Pr = 0.025$. Blue (dark gray) dots are the MLE calculated from XPPAUT, and black lines are the linear fit. (b) Onset of flow reversals obtained from DNS as a function of Q for $Pr = 0.025$.

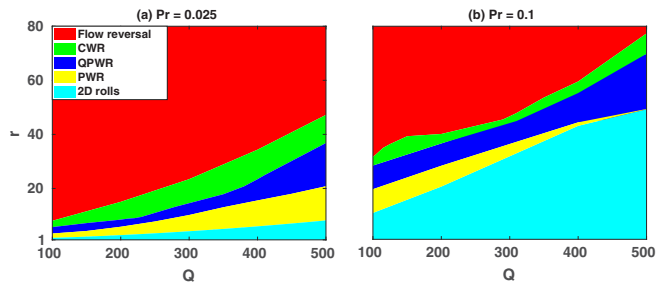


FIG. 7. (a) and (b) display the variation of the different flow regimes, namely, 2D rolls (cyan or lighter gray regions), PWR (yellow or white regions), QPWR (blue or dark gray regions), CWR (green or light gray regions), and the regions where reversals occur (red or medium gray regions) on the Q - r plane for two different Pr as obtained from the model.

becomes vanishingly small. Also, the onset of flow reversals for fixed Q moves towards the higher r , and a phenomenological similarity with Q is observed in the sense that the increment in Pr also delayed the flow reversal phenomena.

VI. CONCLUSIONS

In conclusion, we have studied the nonlinear dynamics of flow reversals appearing in low-Pr Rayleigh-Bénard convection in the presence of an external uniform horizontal magnetic field. We have performed direct numerical simulations of the governing equations and low-dimensional modeling of the system for this purpose. We have characterized an attractor-merging crisis which is found to cause the

random flow reversals in the system. We have also shown that the increment in the strength of the magnetic field and Pr delay the flow reversal phenomena until higher Rayleigh numbers and enhance the region of two-dimensionality. These results might be applicable to various industrial applications in which efforts are made to minimize the effect of flow reversals.

ACKNOWLEDGMENTS

P.P. acknowledges support from the SERB (DST, India; Grant No. EMR/2015/001680). M.G. is supported by the INSPIRE program of the DST, India (Code No. IF150261). The authors thank P. Ghosh, L. Sharma, and S. Mandal for their useful suggestions and the anonymous referees for their insightful comments.

-
- [1] S. Hanasoge, L. Gizon, and K. R. Sreenivasan, *Annu. Rev. Fluid Mech.* **48**, 191 (2016).
 - [2] P. A. Davidson, X. He, and A. J. Lowe, *Mater. Sci. Technol.* **16**, 699 (2000).
 - [3] E. van Doorn, B. Dhruva, K. R. Sreenivasan, and V. Cassella, *Phys. Fluids* **12**, 1529 (2000).
 - [4] S. Chandrasekhar, *Hydrodynamic and Hydromagnetic Stability* (Cambridge University Press, Cambridge, 1961).
 - [5] G. Ahlers, S. Grossmann, and D. Lohse, *Rev. Mod. Phys.* **81**, 503 (2009).
 - [6] F. Bouchet and E. Simonnet, *Phys. Rev. Lett.* **102**, 094504 (2009).
 - [7] K. Sugiyama, R. Ni, R. J. A. M. Stevens, T. S. Chan, S.-Q. Zhou, H.-D. Xi, C. Sun, S. Grossmann, K.-Q. Xia, and D. Lohse, *Phys. Rev. Lett.* **105**, 034503 (2010).
 - [8] F. Chillà and J. Schumacher, *Eur. Phys. J. E* **35**, 1 (2012).
 - [9] M. Chandra and M. K. Verma, *Phys. Rev. Lett.* **110**, 114503 (2013).
 - [10] M. K. Verma, S. C. Ambhire, and A. Pandey, *Phys. Fluids* **27**, 047102 (2015).
 - [11] A. Pandey, M. K. Verma, and M. Barma, *Phys. Rev. E* **98**, 023109 (2018).
 - [12] T. Yanagisawa, Y. Yamagishi, Y. Hamano, Y. Tasaka, and Y. Takeda, *Phys. Rev. E* **83**, 036307 (2011).
 - [13] T. Yanagisawa, Y. Hamano, T. Miyagoshi, Y. Yamagishi, Y. Tasaka, and Y. Takeda, *Phys. Rev. E* **88**, 063020 (2013).
 - [14] T. Yanagisawa, Y. Hamano, and A. Sakuraba, *Phys. Rev. E* **92**, 023018 (2015).
 - [15] M. Mannattil, A. Pandey, M. K. Verma, and S. Chakraborty, *Eur. Phys. J. B* **90**, 259 (2017).
 - [16] P. Pal, P. Wahi, S. Paul, M. K. Verma, K. Kumar, and P. K. Mishra, *Europhys. Lett.* **87**, 54003 (2009).
 - [17] P. Pal and K. Kumar, *Eur. Phys. J. B* **85**, 201 (2012).
 - [18] Y. Nandukumar and P. Pal, *Europhys. Lett.* **112**, 24003 (2015).
 - [19] A. Basak and K. Kumar, *Chaos* **26**, 123123 (2016).
 - [20] C. Grebogi, E. Ott, and J. A. Yorke, *Phys. D (Amsterdam, Neth.)* **7**, 181 (1983).
 - [21] C. Grebogi, E. Ott, F. Romeiras, and J. A. Yorke, *Phys. Rev. A* **36**, 5365 (1987).
 - [22] C. L. Pando L., G. Perez, and H. A. Cerdeira, *Phys. Rev. E* **48**, 196 (1993).
 - [23] A. Magauer and S. Banerjee, *IEEE Trans. Circuits Syst., I: Fundam. Theory Appl.* **47**, 254 (2000).
 - [24] V. N. Chizhevsky, R. Vilaseca, and R. Corbalán, *Phys. Rev. E* **61**, 6500 (2000).
 - [25] E. L. Rempel and A. C.-L. Chian, *Phys. Rev. E* **71**, 016203 (2005).
 - [26] A. C.-L. Chian, F. A. Borotto, E. L. Rempel, and C. Rogers, *Chaos, Solitons Fractals* **24**, 869 (2005).
 - [27] M. Ghosh, P. Ghosh, Y. Nandukumar, and P. Pal, *Phys. Fluids* **32**, 024110 (2020).
 - [28] M. K. Verma, A. Chatterjee, K. S. Reddy, R. K. Yadav, S. Paul, M. Chandra, and R. Samtaney, *Pramana* **81**, 617 (2013).
 - [29] A. Libchaber, S. Fauve, and C. Laroche, *Phys. D (Amsterdam, Neth.)* **7**, 73 (1983).
 - [30] P. Pal, M. Ghosh, A. Banerjee, P. Ghosh, Y. Nandukumar, and L. Sharma, in *Dynamics and Control of Energy Systems* (Springer, Singapore, 2020), pp. 385–408.
 - [31] B. Ermentrout, *Simulating, Analyzing, and Animating Dynamical Systems: A Guide to XPPAUT for Researchers and Students* (SIAM, 2002).
 - [32] S. Paul, K. Kumar, M. K. Verma, D. Carati, A. K. De, and V. Eswaran, *Pramana* **74**, 75 (2010).
 - [33] S. Fauve, C. Laroche, and A. Libchaber, *J. Phys., Lett.* **45**, 101 (1984).
 - [34] M. K. Verma, *Physics of Buoyant Flows: From Instabilities to Turbulence* (World Scientific, Singapore, 2018).
 - [35] V. Mehra and R. Ramaswamy, *Phys. Rev. E* **53**, 3420 (1996).